

Article

Experimental Investigation of Thermal Runaway Characteristics of Large-Format Li(Ni_{0.8}Co_{0.1}Mn_{0.1})O₂ Battery under Different Heating Powers and Areas

Jingru Huang ¹, **Zhuwei Fan** ¹, **Chengshan Xu** ², **Fachao Jiang** ^{1,*} and **Xuning Feng** ²¹ College of Engineering, China Agricultural University, Beijing 100083, China; huangjr@cau.edu.cn (J.H.); 2017307070302@cau.edu.cn (Z.F.)² State Key Laboratory of Automotive Safety and Energy, Tsinghua University, Beijing 100084, China; xcs_pcg@mail.tsinghua.edu.cn (C.X.); fxn17@tsinghua.edu.cn (X.F.)

* Correspondence: jfachao@cau.edu.cn

Abstract: This study experimentally investigates the effects of different heating powers and areas on the jet behavior and thermal runaway (TR) of 75 Ah LiNi_{0.8}Co_{0.1}Mn_{0.1}O₂ pouch lithium-ion batteries (LIBs) in an open environment. TR, a critical safety concern for LIBs, can occur under overheating conditions. The TR behavior of LIBs was characterized by flame behavior, temperature characteristics, mass variation, jet dynamics, and residue formations. The results reveal that the heating power density primarily influences the time to initiate TR. Lower power densities extend the heating time and require higher energy to induce TR, thereby exerting a more considerable impact on the battery. The heating area predominantly affects the input energy and the extent of damage. Larger areas lead to more stable jet flames, consistent peak temperatures ranging between 1000 °C and 1300 °C, and mass loss ratios ranging from 44% to 53% compared to 43% to 47% for small-area heaters. These findings provide references for the safety design of battery assemblies and the prevention of TR propagation, contributing to the safer monitoring of LIBs.



Citation: Huang, J.; Fan, Z.; Xu, C.; Jiang, F.; Feng, X. Experimental Investigation of Thermal Runaway Characteristics of Large-Format Li(Ni_{0.8}Co_{0.1}Mn_{0.1})O₂ Battery under Different Heating Powers and Areas. *Batteries* **2024**, *10*, 241. <https://doi.org/10.3390/batteries10070241>

Academic Editors: Wojciech Mrozik and Carlos Zieberth

Received: 15 April 2024

Revised: 6 June 2024

Accepted: 2 July 2024

Published: 4 July 2024



Copyright: © 2024 by the authors. Licensee MDPI, Basel, Switzerland. This article is an open access article distributed under the terms and conditions of the Creative Commons Attribution (CC BY) license (<https://creativecommons.org/licenses/by/4.0/>).

1. Introduction

Lithium-ion batteries are extensively utilized in electric vehicles due to their high energy density, long cycle life, and low self-discharge rates [1–4]. However, under conditions of mechanical abuse [5–8], electrical abuse [9,10], and thermal abuse [11,12], the internal active materials of lithium-ion batteries may decompose or react with each other, ultimately leading to thermal runaway [13–16]. Therefore, understanding the mechanisms and principles of thermal runaway in lithium-ion batteries is crucial for developing strategies to enhance their safety under overheating conditions [17–20]. Feng et al. [21] identified and analyzed three characteristic temperatures during the thermal runaway process through extensive experimental data, summarizing and proposing temperature indicators for assessing the safety of lithium-ion batteries. Zheng et al. [22] investigated the exothermic reaction mechanism between lithiated graphite and electrolytes through DSC and evolved gas analysis, finding that the main sources of heat production are the decomposition of the SEI film, reactions between lithiated graphite and the electrolyte, and reactions between lithiated graphite and the binder.

From a macroscopic perspective, the primary mechanism of thermal abuse involves disrupting the balance between heat absorption and dissipation in batteries through external heating. Focusing on the heating variables, the main considerations are the power density of heating and the location of heating. Huang et al. [23] investigated the effects of heating power and state of charge (SOC) on the thermal runaway of batteries, triggering thermal runaway in a 94 Ah LiNi_{1/3}Co_{1/3}Mn_{1/3}O₂ prismatic battery with different

heating power densities. Compared to the SOC, the impact of heating density was more significant; higher heating power densities led to shorter times required to trigger thermal runaway, less heat absorbed by the battery, and slower internal heat propagation. Zhou et al. [24] studied the impact of thermal runaway characteristics on lithium iron phosphate batteries under different heating powers using copper slug battery calorimetry, finding that the maximum temperature and internal heat generation of the battery did not increase monotonically with heating power, but peaked at 100 W. Zhou et al. [25] researched the effect of heating trigger locations on the thermal runaway of 27 Ah prismatic lithium-ion batteries, discovering that the thermal conductivity rates on the side and bottom surfaces were faster, leading to more intense thermal runaway phenomena. Jin et al. [26] explored the combined effects of heating power and heating area on triggering thermal runaway and studied the mechanism of heat-transfer-induced thermal runaway through modeling, finding that at the same heating power, higher heating power densities and smaller heating areas resulted in shorter times to trigger TR. Within the testing standard (GB/T 38031) [27], side heating is widely used in triggering the TR of the battery.

During the thermal runaway process of lithium-ion batteries, the internal reactions generate increasing amounts of gas, and in the case of prismatic batteries, multiple eruptions typically occur during thermal runaway. Wang et al. [28] induced thermal runaway in a 50 Ah NCM622 prismatic battery through lateral heating, finding a negative correlation between the flame ejection temperature and the height position of the flame, while the state of charge of the battery affected the maximum temperature of the battery jet, manifesting at the safety valve's location. To observe the characteristics of the battery thermal runaway eruption process, Zou et al. [29] conducted a side-heating-triggered thermal runaway experiment on a 38 Ah ternary lithium-ion prismatic battery, recording and analyzing the jet behavior in terms of speed and temperature. Despite the existing studies on the impact of heating power on thermal runaway (TR) characteristics and the jet behavior of prismatic batteries under side-heating conditions, there is still a lack of analysis on the effects of heating power density and heating area on the TR and jetting behavior of large-format pouch lithium-ion batteries (LIBs). Furthermore, there is insufficient research on the comprehensive relationship between heating time, input energy, heating power, and heating area for triggering TR. In real-world situations, the heating power and heating area acting on a battery during an overheating event can be highly variable and random. Additionally, during TR propagation, the heating power exerted on adjacent cells through thermal conduction and flame radiation from a pouch cell undergoing TR is often very high and diverse. Enhancing the understanding of the relationship between heating power, heating area, and TR induced by overheating can aid battery and module developers in designing effective strategies against TR initiation and propagation. The jet temperature of the battery is one of the key fundamental parameters in the design of battery thermal management systems (BTMSs) for automotive applications. Moreover, the current understanding of localized heating and the resulting jetting behavior in large-format pouch batteries is limited and requires further exploration. This study also aims to deepen the understanding of jetting behavior in large-format pouch LIBs, providing references for the safe design and hazard prevention of LIBs.

In this work, the effects of different heating areas and power densities of heaters on the thermal runaway characteristics of 75 Ah Li(Ni_{0.8}Co_{0.1}Mn_{0.1})O₂ pouch lithium-ion batteries are systematically investigated through experiments. Under various heating conditions, the behavior of battery flames, the characteristics of battery surface temperatures, jetting features, mass changes, and the morphology of battery residues are analyzed. The experimental results demonstrated that reducing the heating area while increasing the power density during lateral heating experiments can decrease the energy input and time required to induce thermal runaway in batteries.

2. Experimental

2.1. Battery Information

A commercial rectangular pouch lithium-ion battery was investigated in this paper. The specific details of the battery are summarized in Table 1. The cathode material is NCM (Ni:Co: Mn = 8:1:1), and the anode material is graphite. The nominal capacity and voltage of the battery are 75 Ah and 3.68 V, respectively, with dimensions of $542 \times 101 \times 8.21$ mm. The battery weighs 1070 g and has an energy density of 267 Wh/kg. A Neware battery cycler was employed to discharge the battery to 2.8 V at a constant current of 1/3C (25A), followed by a 1 h rest, then charged to 4.2 V (SOC = 100%) using constant current (1/3C) and constant voltage (4.2 V, 1/20C cut-off current). At this point, the state-of-charge of each battery was charged to 100% SOC before the tests, and the LIB was maintained for 24 h to ensure its stability.

Table 1. Some specific information of the tested LIB.

Parameters	Specification
Cathode active material	Lithium nickel manganese cobalt ($\text{LiNi}_{0.8}\text{Co}_{0.1}\text{Mn}_{0.1}\text{O}_2$)
Anode active material	Graphite
Nominal capacity (Ah)	75
Nominal voltage (V)	3.68
Maximum cut-off voltage (V)	4.2
Minimum cut-off voltage (V)	2.8
Geometry (mm)	$542 \times 101 \times 8.21$
Mass (g)	1070
Energy density (Wh/kg)	267

2.2. Experimental Settings

To monitor the temperature changes on the battery surface during TR, seven K-type thermocouples with a diameter of 1 mm were placed on the surface, labeled TC1 to TC7, as illustrated in Figure 1. The thermocouple TC4, located at the center of the heating area, was used to capture the temperature rise curve on the battery surface during the heating process. This enabled the determination of the start and end moments of heating, as well as the surface temperature immediately before TR. TC2 and TC6, positioned at the center of the heating side and the back center of the battery, respectively, were used to measure the time interval between the front and back surfaces during TR, thereby calculating the propagation speed in the thickness direction of the battery. TC1, TC3, TC5, and TC7 were arranged at the battery tab locations. By comparing the temperature rise curves at the center and tab locations, the lateral propagation speed on the same surface could be estimated. Additionally, the battery's voltage drop was recorded and analyzed to examine the relationship between the voltage decline and the temperature rise over time.

After the placement of surface thermocouples on the battery, a heater was positioned at the center area of the pouch battery's sealing edge, as shown in Figure 2a. Due to the heater's relatively small area compared to the battery surface, a thermal insulating layer was wrapped around the heater to ensure an even distribution of force across the battery. This assembly was then clamped between two mica boards, with the external side held by a steel fixture comprising two stainless steel boards and eight bolts tightened in diagonal sequence, applying a torque of 5 N·m. Figure 2b shows the physical setup of the battery and fixture. For TR experiments, thermocouples were placed directly above the heating area to measure the temperature distribution of the ejecting flames at various heights from the battery surface, with temperature measurement points set every 10 cm, totaling ten thermocouples. A camera was positioned 3 m away from the likely area of TR to record the process, as shown in Figure 2c, while a thermal imager observed the ambient temperature distribution during the TR event. Figure 2d shows the physical picture of the experimental setup.

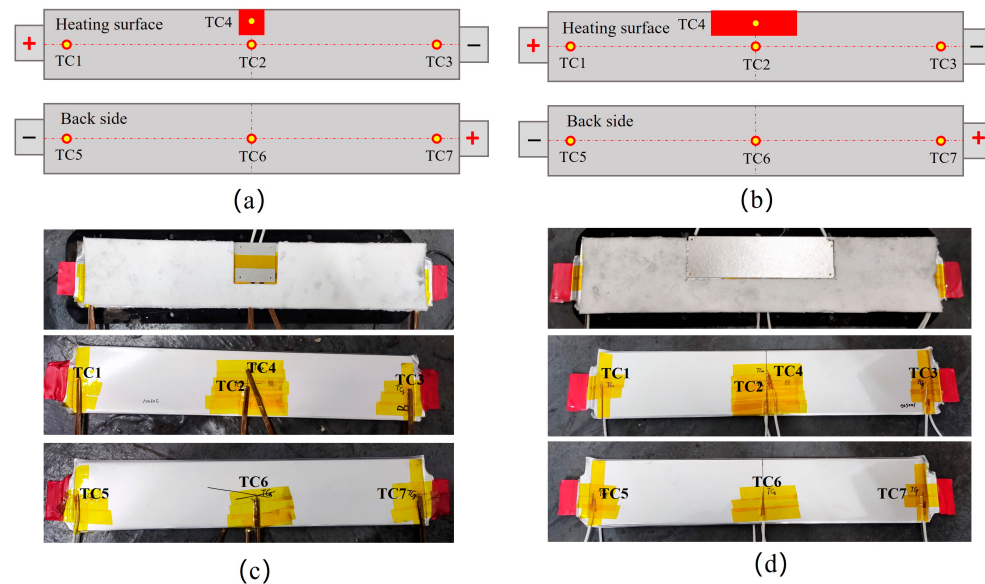


Figure 1. Schematic illustration of the thermocouple arrangement. (a) Schematic of thermocouple layout with a small heater. (b) Schematic of thermocouple layout with a large heater. (c) Physical depiction of thermocouple arrangement with a small heater. (d) Physical depiction of thermocouple arrangement with a large heater.

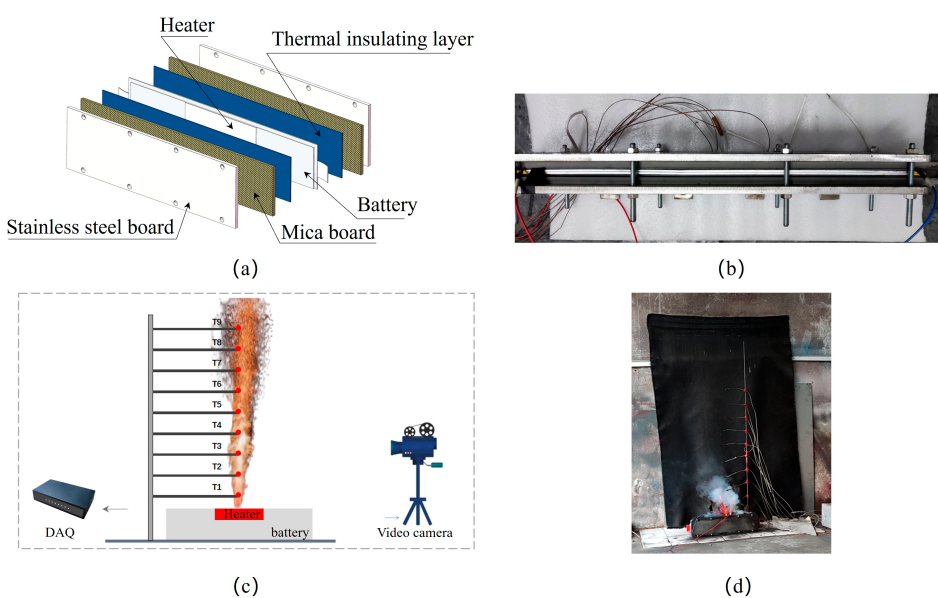


Figure 2. Experimental setup. (a) Schematic figure of battery and fixture setup. (b) Physical picture of battery and fixture setup. (c) Structural diagram of experimental setup. (d) Physical picture of experimental setup.

In this study, the heater sizes of $6 \times 6 \text{ cm}^2$ and $21 \times 6 \text{ cm}^2$ were employed, with three heating power densities of 8.33, 5, and 2.38 W/cm^2 for each heater size, to characterize the combined effects of heating power and heating area. The test configurations and conditions are detailed in Table 2.

Table 2. Summary of total tests.

Experiment No.	SOC	Heating Area [cm ²]	Heating Power Density [W/cm ²]
1	100%	6 × 6	8.33
2	100%	6 × 6	5
3	100%	6 × 6	2.38
4	100%	21 × 6	8.33
5	100%	21 × 6	5
6	100%	21 × 6	2.38

3. Results and Discussion

3.1. Phenomenon Observations

Figure 3 depicts the typical fire behaviors of lithium-ion batteries under TR conditions with various heating setups, while Figure 4 shows thermal imaging of the battery and its surroundings during TR. When a small heating area ($6 \times 6 \text{ cm}^2$) and a heating power density of 2.38 W/cm^2 were used, the battery did not undergo TR, thus no battery venting occurred. In the remaining experiments, the stages leading to battery TR were similar and can be divided into four distinct phases: (I) battery casing breach and directed jetting, (II) intense ejection around the battery, (III) fierce combustion, and (IV) gradual flame extinguishment.

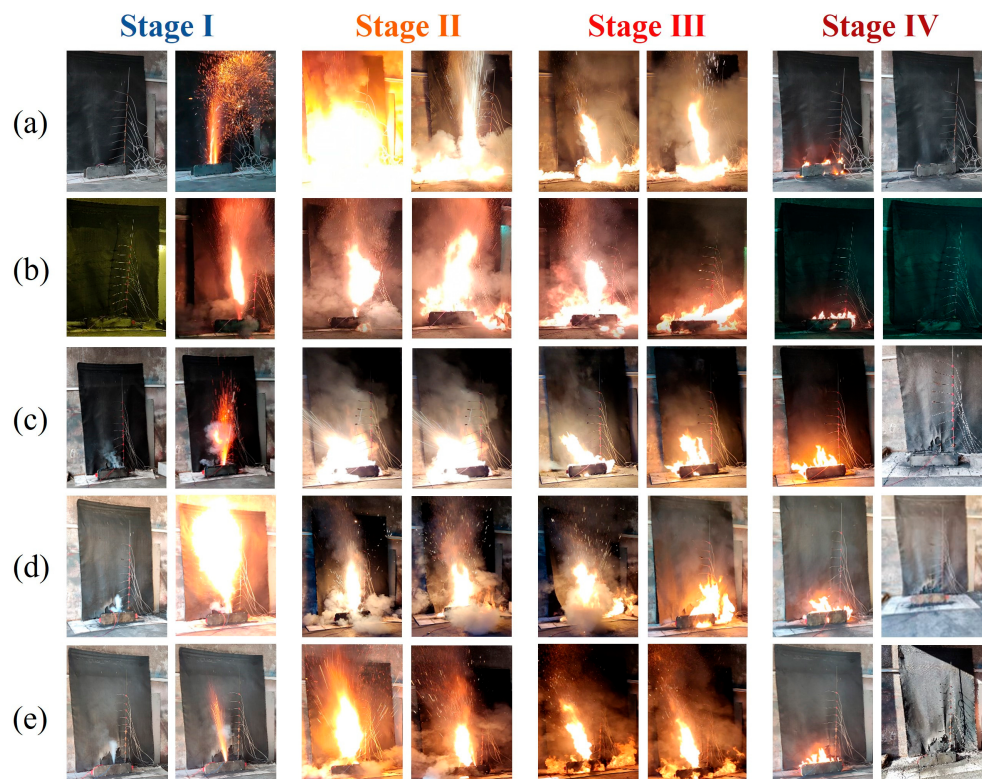


Figure 3. Fire behavior of LIBs under different heating methods. (a) Experiment No. 1, (b) Experiment No. 2, (c) Experiment No. 4, (d) Experiment No. 5, and (e) Experiment No. 6.

The first phase involved the battery's heating face breaching in the heated area, ejecting an electrolyte, which ignited and formed a small flame. This phase was characterized by directional jetting due to the internal pressure being released through the breach, which intensified as the electrolyte was rapidly ejected, enlarging the damaged area. In Tests 1 and 4, the directional jetting phase lasted about 1 s for small heating areas at a power density of 8.33 W/cm^2 , extending to 3 s for large heating areas at the same power density, indicating that larger heating areas resulted in longer directional jetting phases at the same

power density. The height of the flame jetting could reach 1.5 m. In the second phase, as the TR area spread, the battery's surface aluminum–plastic film gradually burned away, and other weak areas of the battery, such as the tabs, began to eject electrolytes and flames, accompanied by roaring sounds and the ejection of particles, possibly containing graphite and other metal compounds. The third phase was marked by intense combustion, typically lasting about 10 s, followed by the final phase where the flames gradually diminished and extinguished.

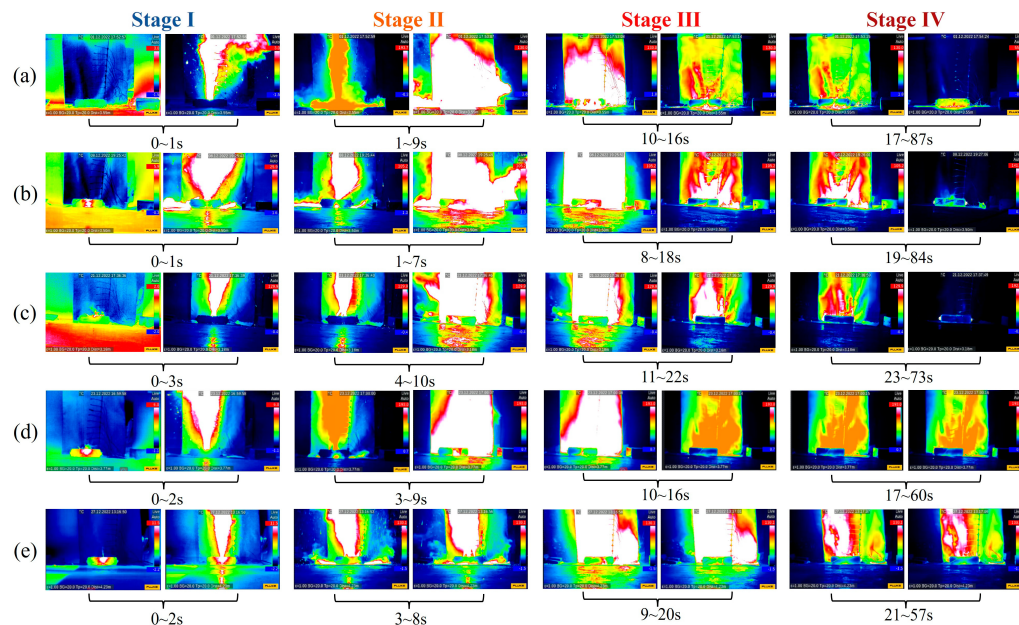


Figure 4. Thermal imaging of LIBs under different heating methods. (a) Experiment No. 1, (b) Experiment No. 2, (c) Experiment No. 4, (d) Experiment No. 5, and (e) Experiment No. 6.

3.2. Temperature Response and Energy Input

Temperature is identified as a critical parameter in characterizing the TR process and heat generation [30,31]. T_{onset} is the triggering temperature of the battery's TR, which is defined as a critical point where a rapid temperature rise begins. The threshold for the rate of temperature rise was taken as $1 \text{ }^{\circ}\text{C}/\text{s}$. The onset temperatures (T_{onset}) for TR at various heating conditions and locations on the battery's heated surface were in the range of $231\text{--}373 \text{ }^{\circ}\text{C}$ for the center of the heating area ($T_{\text{onset},4}$), in the range of $22\text{--}32 \text{ }^{\circ}\text{C}$ near the tabs ($T_{\text{onset},3}$), and in the range of $37\text{--}85 \text{ }^{\circ}\text{C}$ on the opposite back surface ($T_{\text{onset},5}$).

In this section, Δt and v are introduced to assess the severity of TR, where Δt_1 is defined as the time interval between the onset temperatures $T_{\text{onset}4}$ and $T_{\text{onset}3}$ on the battery's heated surface. Δt_2 is defined as the time interval between the heated surface's onset temperature $T_{\text{onset}3}$ and the back surface's onset temperature $T_{\text{onset}5}$. The TR propagation speed (v) can be calculated using Equation (1), where $L(1)$ represents the distance between TC2 and TC3, and $L(2)$ corresponds to the battery's thickness. $v_{(1)}$ and $v_{(2)}$ are, respectively, defined as the surface spread rate and thickness spread rate.

$$V_{(i)} = \frac{L(i)}{\Delta t(i)}, i \in \{1, 2\} \quad (1)$$

As illustrated in Table 3, using a small heating pad with a heating power density of 8.33 W/cm^2 to initiate TR in a battery, the transition from the start of heating to the onset of TR took approximately 1 min. The heat spread from the central heating area to the back surface near the battery tabs in about 8.2 s, with a surface propagation speed of approximately 57.96 mm/s . In contrast, the propagation speed through the battery's thickness was 2.16 mm/s , indicating faster heat spread on the side with the heater compared

to the direction of battery thickness. The internal heat propagation speed ranged between 1.80 and 3.91 mm/s, suggesting slower internal heat transfer, possibly due to the insulating properties of the battery's internal materials or structural barriers to heat flow. Significant fluctuations in thermocouple readings between the heater and battery were observed due to the TR jet.

Table 3. Summary of measured critical parameters for batteries during TR.

Experiment No.	Heater Heating Time (s)	Heater Input Energy (kJ)	Surface Spread Rate (mm/s)	Thickness Spread Rate (mm/s)
1	50.8	15.2	57.96	2.16
2	180.3	32.5	52.04	1.87
4	51.8	54.4	47.22	2.57
5	108.6	68.4	70.83	3.91
6	358.1	107.4	47.22	2.22

When using a small heating pad with a power density of 5 W/cm^2 , the interval from the onset of heating to the initiation of TR in the battery extended to 180.3 s, tripling the heating duration compared to a power density of 8.33 W/cm^2 , and increasing the energy introduced to 32.5 kJ. The heat spread from the central heating area to the back surface near the battery tabs in approximately 9.3 s, with a surface spread speed of about 52.04 mm/s and a thickness spread speed that increased to 1.87 mm/s. Similar to the previous experiment, the heating power density primarily affected the time required to trigger TR in the battery. For a large heating area ($21 \times 6\text{ cm}^2$) with the same power density of 8.33 W/cm^2 , the TR initiation time was 51.8 s, with an energy input of 54.4 kJ. The battery exhibited a surface spread speed of 47.22 mm/s and a thickness spread speed of 2.57 mm/s. The increase in the heating area did not significantly reduce the time to trigger TR but led to a higher energy input, resulting in more intense TR behavior. This suggests that while the size of the heating area had a minimal effect on the rate of the internal spread of TR within a single cell, larger heating areas contributed to higher energy inputs and more severe TR manifestations. When using a heating power density of 2.38 W/cm^2 with a small heating area ($6 \times 6\text{ cm}^2$), TR did not occur in the battery. As observed from Figure 5, the rate of temperature increase on the battery surface began to decrease 358.8 s into heating. The repetition of the experiment under the same conditions resulted in no TR, suggesting that the lower heating power of the pad allowed for an equilibrium to form between the heated and unheated regions of the battery and the surrounding air. In contrast, with larger heaters, this thermal equilibrium was disrupted, leading to TR initiation. With the large heater set to the minimum power density of 2.38 W/cm^2 , the time to trigger TR significantly increased to 358.1 s, introducing the highest energy input to the battery, reaching 107.4 kJ.

Averaging the peak surface temperature values ($T_{ave-max}$) from multiple experiments of TR induced by heaters of the same heating area, as shown in Figure 6, revealed that the highest temperatures were measured by the TC4 thermocouple at the contact surface between the heater and the LIBs in small heating areas, with an average of $1201.4\text{ }^\circ\text{C}$. This phenomenon was primarily due to the intense reaction and jetting occurring in the battery area near the thermocouple after heater activation. On the battery surface, the distribution of peak temperature values appeared random; however, thermocouples located around the heating area registered higher temperatures, whereas temperatures near the battery end, near the positive and negative terminals, were comparatively lower. For lithium-ion batteries in large heating areas during TR, the temperature characteristics were similar to those in small heating areas but with differences. The highest temperatures still occurred near the TC4 thermocouple in the heating area, averaging $1018.45\text{ }^\circ\text{C}$. This indicates that temperatures in the battery's direct heating zone were significantly higher than in other areas. Following closely was the center of the battery's large surface area, where the heater was placed, with temperatures at the battery ends, near the thermocouples, being similar.

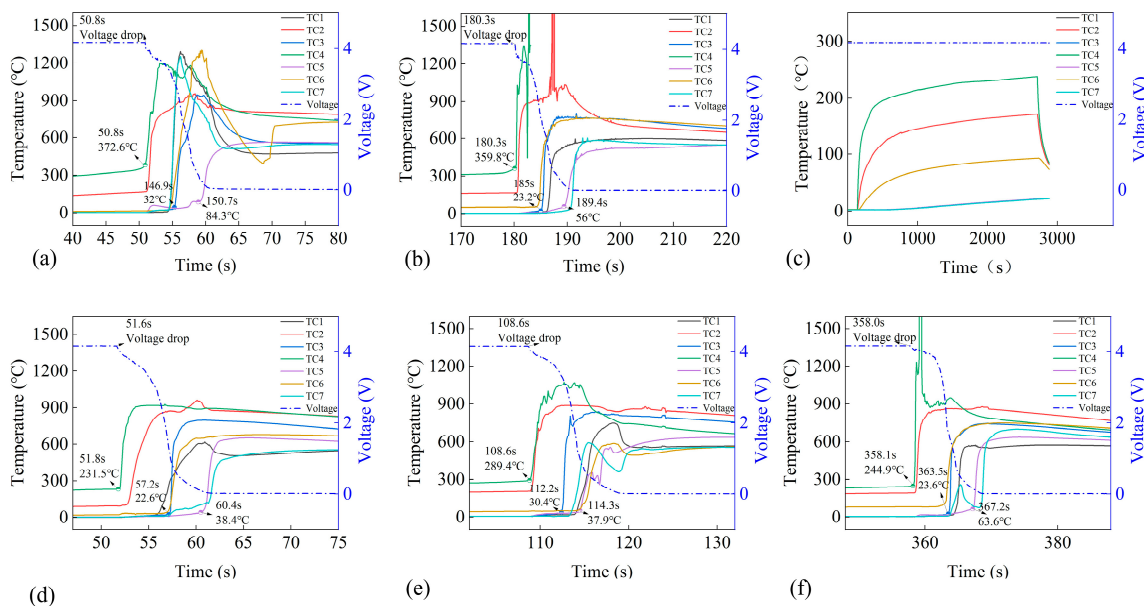


Figure 5. The surface temperature and voltage for LIBs in OS tests. **(a)** Experiment No. 1, **(b)** Experiment No. 2, **(c)** Experiment No. 3, **(d)** Experiment No. 4, **(e)** Experiment No. 5, and **(f)** Experiment No. 6.

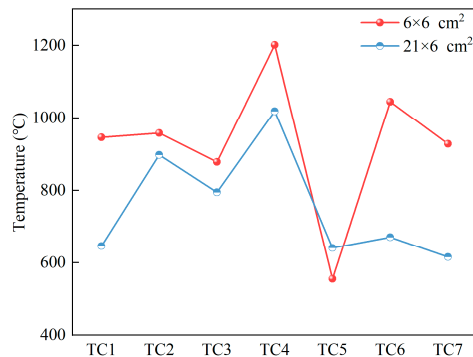


Figure 6. Average of the peak surface temperatures of the battery in each experiment under a heater with the same heating area.

3.3. Jet Temperature

From the thermal imaging and jet temperature distribution graphs, it is observed that during the initial phase of TR, the battery exhibited a phase of directional jetting with relatively uniform flames. However, as TR progressed, the surrounding aluminum–plastic film of the battery became damaged, leading to more disordered flame ejection. As shown in Figure 7, with a heating area of $6 \times 6 \text{ cm}^2$, the temperature rise due to TR occurred in approximately 5 s, with a stable jetting duration of about 1–2 s. The peak temperatures at measurement points above the battery generally ranged between 1000 and 1350 °C. Temperatures at points within 50 cm above the battery's vent were similar, with the peak temperatures beginning to decline as the distance from the battery increased, noticeably beyond 50 cm. For a larger heating area of $21 \times 6 \text{ cm}^2$, the stable jetting duration extended to around 5 s. Larger heating areas resulted in longer peak durations, and the temperature distribution pattern resembled that of smaller heaters, with maximum values within 30 cm above the ejection point showing little difference, generally ranging from 1000 to 1300 °C. The decline in peak temperatures measured by thermocouples became apparent beyond 40 cm from the battery.

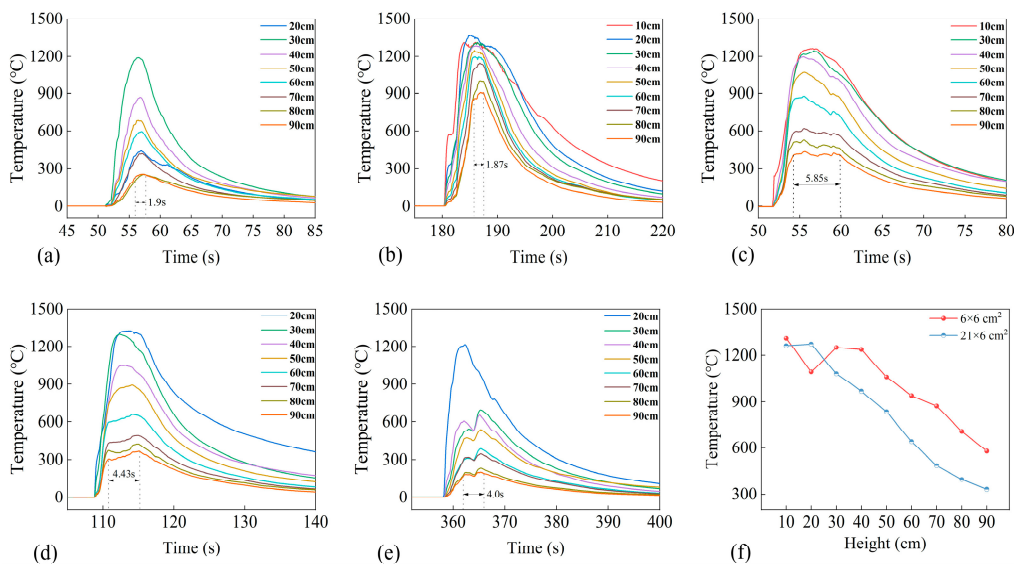


Figure 7. TR jet temperature curves of the battery. **(a)** Experiment No. 1, **(b)** Experiment No. 2, **(c)** Experiment No. 4, **(d)** Experiment No. 5, **(e)** Experiment No. 6, and **(f)** average jet temperature at each measurement point in each experiment under heaters with the same heating area.

3.4. Mass Loss and Combustion Residues

3.4.1. Mass Loss and Mass Loss Ratio

In addition to summarizing battery temperature characteristics and jet temperatures, this study also compiled data on mass loss and mass loss ratios for all tests, as indicated in Figure 8. For batteries undergoing TR triggered by a small heater at a power density of 8.33 W/cm^2 , the mass loss ratio was 43.5%, and at 5 W/cm^2 , it was 45.9%, with mass loss ratios ranging between 43% and 46%. Increasing the heater's power density led to a reduction in battery mass loss, with the period for voltage drop across different power densities remaining consistent at 9–10 s, indicating the minimal impact of heating power on the duration of voltage decline. Jetting duration during TR also stayed around 10 s, allowing for an estimated average mass flow rate of 45–52 g/s during the battery ejection phases. For large heating areas, the pattern of mass loss during TR was similar to that with small heaters, but the larger heater's higher energy input resulted in more intense jetting and increased mass loss, ranging between 45% and 52%. Notably, the same power density of 2.38 W/cm^2 in a small heating area did not trigger TR.

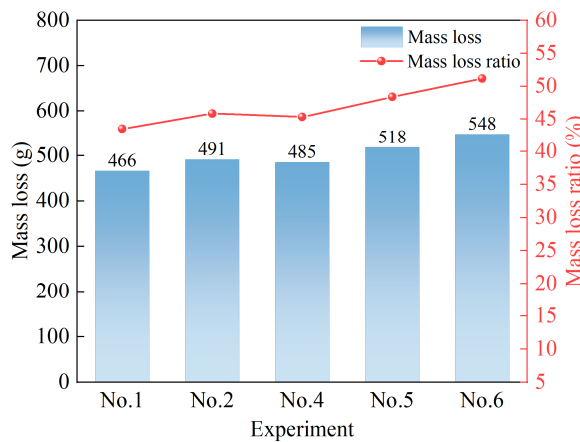


Figure 8. Mass loss and mass loss ratio of LIB.

3.4.2. Analysis of Battery Combustion Residues

The morphology of the residues from pouch batteries with a heating area of $6 \times 6 \text{ cm}^2$ after TR, as shown in Figure 9, indicates that heating power did not significantly affect the damage patterns of the battery. The damage was primarily localized to the area directly affected by the heater, where clear traces of gas flow channels on the battery surface could be observed. The structure of the battery's non-heated areas remained relatively intact. When the heating area was $21 \times 6 \text{ cm}^2$, TR caused more severe damage, with a broader damaged area compared to the smaller heating area. Damage in the larger heating area was not only more extensive but also deeper, with more evident formation of gas flow channels, suggesting that the energy release and internal pressure increase from TR had a more intense impact on the battery structure in larger heating areas. The condition of the residues showed significant swelling and rupture of the aluminum–plastic film in the heated areas, indicating rapid increases in internal pressure and a swift release of high-temperature gases.

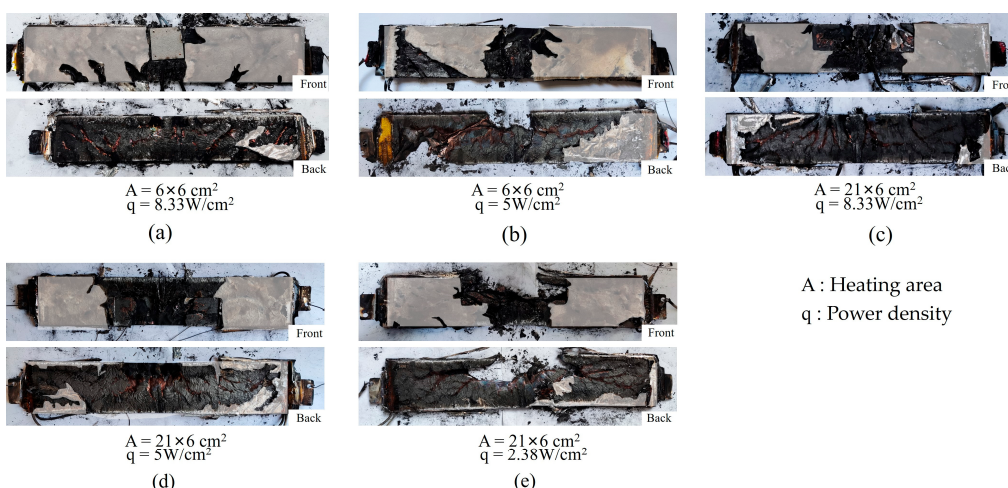


Figure 9. Comparison of LIB morphology after TR. (a) Combustion residues from Experiment No. 1, (b) combustion residues from Experiment No. 2, (c) combustion residues from Experiment No. 4, (d) combustion residues from Experiment No. 5, and (e) combustion residues from Experiment No. 6.

After local TR occurs within a single LIB, the generated heat is transferred to the unreacted areas through thermal conduction via metal current collectors and active materials, as well as through convective heat transfer by the movement of internal gases. This leads to the propagation of TR within the cell [32]. As demonstrated in Figure 10, two distinct regions can be observed during the TR process of a pouch cell: the TR area, marked in red, indicating where the exothermic reactions have completed, resulting in elevated temperatures, and the normal area, depicted in blue, where TR has not occurred, and the temperatures remain near ambient conditions. There exists a transition boundary between the TR area and the normal area known as the thermal runaway front (TRF). As TR progresses from the affected area into the normal area, the TRF advances, converting the normal area into a TR area.

When the heating power density remains constant, a larger heating area due to its more extensive influence and higher input energy leads to increased heat accumulation and dispersion across a broader region. This widespread heating causes a greater portion of the battery to reach the critical threshold for thermal runaway simultaneously, thereby initiating thermal runaway reactions over a larger area and resulting in more extensive damage. Notably, even with the same heating power density of 2.38 W/cm^2 , the smaller heating area failed to trigger TR within the battery. This observation underscores the impact of the heating area on the onset and propagation of TR, revealing that a larger heating area can significantly escalate the spread and severity of thermal events compared to a smaller area.

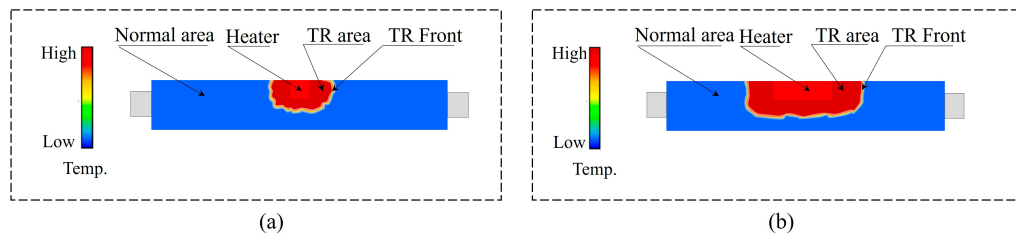


Figure 10. Comparative illustration of the thermal runaway front (TRF) during thermal runaway (TR) in a LIB with different heater sizes. (a) TRF development with a small heating area and (b) TRF development with a large heating area.

4. Conclusions

This experimental study on a 75 Ah $\text{LiNi}_{0.8}\text{Co}_{0.1}\text{Mn}_{0.1}\text{O}_2$ pouch LIB in open space involved the systematic documentation and analysis of flame behavior, temperature characteristics, mass variation, jet behavior, and combustion residues. Employing heaters of two different sizes with three varying heating power densities, the study explored their effects on the TR characteristics and jet behavior of the pouch LIBs. The findings revealed that localized heating led to internal gas accumulation and rupture at the battery's weaker sections. As the heating power increased, the time to trigger thermal runaway (TR) decreased, and the energy introduced by the heater was reduced. At a power density of 8.33 W/cm^2 , the time to initiate TR differed by 1 s between small and large heating areas, with the small area introducing 72.06% less energy than the large area. Therefore, to minimize the energy input and time required for heating-induced TR, experiments with lateral heating could reduce the heater's area while increasing the power density.

The combustion process can be summarized by four stages: battery rupture and directed jetting in the heating area, intense ejection around the battery, severe combustion, and gradual flame extinguishment. Temperature measurements near the heating area were generally higher, while those near the battery's terminals were lower. The surface spread speed of TR was in the range of 48–71 mm/s, and the thickness direction speed was in the range of 1.8–4.0 mm/s. These insights into the combustion stages and temperature distribution are crucial for developing advanced thermal management systems that can better control and prevent TR. The increase in heating power led to reduced mass loss, with TR in small heating areas causing mass loss ratios in the range of 43% to 46%, and in large areas, the range was 45% to 52%. Jet temperatures within 40 cm above the venting point were in the range of 950–1350 °C. With increasing distance from the vent, the peak temperatures recorded at measurement points gradually decreased, showcasing the rapid decay of jet temperatures with distance.

The experimental results offer data for designing protective measures against thermal propagation and help to identify the TR mechanism of LIBs induced by side heating.

Author Contributions: Writing—original draft preparation, J.H.; conceptualization, C.X.; methodology, F.J.; software, Z.F; validation, J.H.; formal analysis, J.H. and Z.F.; investigation, Z.F.; resources, C.X.; data curation, J.H.; writing—review and editing, C.X. and F.J.; visualization, C.X.; supervision, X.F.; project administration, C.X.; funding acquisition, X.F. All authors have read and agreed to the published version of the manuscript.

Funding: This work is supported by the National Key Technologies Research and Development Program Scientific and Technological Strategic Innovation Cooperation (#2022YFE0207900). This work is supported by the Innovative Research Group Project of the National Natural Science Foundation of China [52076121].

Data Availability Statement: The data that supported the findings of this study are available from the corresponding author upon reasonable request.

Acknowledgments: The first author acknowledges Tsinghua University's State Key Laboratory of Automotive Safety and Energy for providing the experimental facilities, and Farasis Energy (Ganzhou, China) Co., Ltd. for providing the experimental materials.

Conflicts of Interest: The authors declare no conflicts of interest.

References

- Zhang, Y.; Wang, H.; Li, W.; Li, C. Quantitative Identification of Emissions from Abused Prismatic Ni-Rich Lithium-Ion Batteries. *eTransportation* **2019**, *2*, 100031. [\[CrossRef\]](#)
- Wei, G.; Huang, R.; Zhang, G.; Jiang, B.; Zhu, J.; Guo, Y.; Han, G.; Wei, X.; Dai, H. A Comprehensive Insight into the Thermal Runaway Issues in the View of Lithium-Ion Battery Intrinsic Safety Performance and Venting Gas Explosion Hazards. *Appl. Energy* **2023**, *349*, 121651. [\[CrossRef\]](#)
- Song, L.; Huang, Z.; Mei, W.; Jia, Z.; Yu, Y.; Wang, Q.; Jin, K. Thermal Runaway Propagation Behavior and Energy Flow Distribution Analysis of 280 Ah LiFePO₄ Battery. *Process Saf. Environ. Prot.* **2023**, *170*, 1066–1078. [\[CrossRef\]](#)
- Ohneseit, S.; Finster, P.; Floras, C.; Lubenau, N.; Uhlmann, N.; Seifert, H.J.; Ziebert, C. Thermal and Mechanical Safety Assessment of Type 21700 Lithium-Ion Batteries with NMC, NCA and LFP Cathodes—Investigation of Cell Abuse by Means of Accelerating Rate Calorimetry (ARC). *Batteries* **2023**, *9*, 237. [\[CrossRef\]](#)
- Mao, B.; Chen, H.; Cui, Z.; Wu, T.; Wang, Q. Failure Mechanism of the Lithium Ion Battery during Nail Penetration. *Int. J. Heat Mass Transf.* **2018**, *122*, 1103–1115. [\[CrossRef\]](#)
- Xu, J.; Mei, W.; Zhao, C.; Liu, Y.; Zhang, L.; Wang, Q. Study on Thermal Runaway Mechanism of 1000 mAh Lithium Ion Pouch Cell during Nail Penetration. *J. Therm. Anal. Calorim.* **2021**, *144*, 273–284. [\[CrossRef\]](#)
- Finegan, D.P.; Tjaden, B.; Heenan, T.M.M.; Jervis, R.; Michiel, M.D.; Rack, A.; Hinds, G.; Brett, D.J.L.; Shearing, P.R. Tracking Internal Temperature and Structural Dynamics during Nail Penetration of Lithium-Ion Cells. *J. Electrochem. Soc.* **2017**, *164*, A3285. [\[CrossRef\]](#)
- Yin, H.; Ma, S.; Li, H.; Wen, G.; Santhanagopalan, S.; Zhang, C. Modeling Strategy for Progressive Failure Prediction in Lithium-Ion Batteries under Mechanical Abuse. *eTransportation* **2021**, *7*, 100098. [\[CrossRef\]](#)
- Ren, D.; Feng, X.; Lu, L.; Ouyang, M.; Zheng, S.; Li, J.; He, X. An Electrochemical-Thermal Coupled Overcharge-to-Thermal-Runaway Model for Lithium Ion Battery. *J. Power Sources* **2017**, *364*, 328–340. [\[CrossRef\]](#)
- Zhang, G.; Wei, X.; Chen, S.; Zhu, J.; Han, G.; Dai, H. Unlocking the Thermal Safety Evolution of Lithium-Ion Batteries under Shallow over-Discharge. *J. Power Sources* **2022**, *521*, 230990. [\[CrossRef\]](#)
- Li, H.; Zhou, D.; Zhang, M.; Liu, B.; Zhang, C. Multi-Field Interpretation of Internal Short Circuit and Thermal Runaway Behavior for Lithium-Ion Batteries under Mechanical Abuse. *Energy* **2023**, *263*, 126027. [\[CrossRef\]](#)
- Özdemir, T.; Ekici, Ö.; Köksal, M. Numerical and Experimental Investigation of the Electrical and Thermal Behaviors of the Li-Ion Batteries under Normal and Abuse Operating Conditions. *J. Energy Storage* **2024**, *77*, 109880. [\[CrossRef\]](#)
- Wang, Q.; Mao, B.; Stoliarov, S.I.; Sun, J. A Review of Lithium Ion Battery Failure Mechanisms and Fire Prevention Strategies. *Prog. Energy Combust. Sci.* **2019**, *73*, 95–131. [\[CrossRef\]](#)
- Xu, C.; Wang, H.; Jiang, F.; Feng, X.; Lu, L.; Jin, C.; Zhang, F.; Huang, W.; Zhang, M.; Ouyang, M. Modelling of Thermal Runaway Propagation in Lithium-Ion Battery Pack Using Reduced-Order Model. *Energy* **2023**, *268*, 126646. [\[CrossRef\]](#)
- Yeon, S.-Y.; Umurov, N.; Lim, S.-H.; Bakenov, Z.; Kim, J.-S.; Kim, S.-S. Thermal Stability and Reduction Mechanism of LiNi_{0.8}Co_{0.1}Mn_{0.1}O₂ and LiNi_{0.5}Co_{0.2}Mn_{0.3}O₂ Cathode Materials Studied by a Temperature Programmed Reduction. *Thermochim. Acta* **2021**, *706*, 179069. [\[CrossRef\]](#)
- Wu, R.; Liu, X.; Zheng, Y.; Li, Y.; Shi, H.; Cheng, X.; Pfleging, W.; Zhang, Y. Unveiling the Intrinsic Reaction between Silicon-Graphite Composite Anode and Ionic Liquid Electrolyte in Lithium-Ion Battery. *J. Power Sources* **2020**, *473*, 228481. [\[CrossRef\]](#)
- Jia, Z.; Qin, P.; Li, Z.; Wei, Z.; Jin, K.; Jiang, L.; Wang, Q. Analysis of Gas Release during the Process of Thermal Runaway of Lithium-Ion Batteries with Three Different Cathode Materials. *J. Energy Storage* **2022**, *50*, 104302. [\[CrossRef\]](#)
- Xu, C.; Fan, Z.; Zhang, M.; Wang, P.; Wang, H.; Jin, C.; Peng, Y.; Jiang, F.; Feng, X.; Ouyang, M. A Comparative Study of the Venting Gas of Lithium-Ion Batteries during Thermal Runaway Triggered by Various Methods. *Cell Rep. Phys. Sci.* **2023**, *4*, 101705. [\[CrossRef\]](#)
- Kisseler, N.; Hoheisel, F.; Offermanns, C.; Frieges, M.; Heimes, H.; Kampker, A. Monitoring of Thermal Runaway in Commercial Prismatic High-Energy Lithium-Ion Battery Cells via Internal Temperature Sensing. *Batteries* **2024**, *10*, 41. [\[CrossRef\]](#)
- Yang, M.; Rong, M.; Pan, J.; Ye, Y.; Yang, A.; Chu, J.; Yuan, H.; Wang, X. Thermal Runaway Behavior Analysis during Overheating for Commercial LiFePO₄ Batteries under Various State of Charges. *Appl. Therm. Eng.* **2023**, *230*, 120816. [\[CrossRef\]](#)
- Feng, X.; Zheng, S.; Ren, D.; He, X.; Wang, L.; Cui, H.; Liu, X.; Jin, C.; Zhang, F.; Xu, C.; et al. Investigating the Thermal Runaway Mechanisms of Lithium-Ion Batteries Based on Thermal Analysis Database. *Applied Energy* **2019**, *246*, 53–64. [\[CrossRef\]](#)
- Zheng, Y.; Shi, Z.; Ren, D.; Chen, J.; Liu, X.; Feng, X.; Wang, L.; Han, X.; Lu, L.; He, X.; et al. In-Depth Investigation of the Exothermic Reactions between Lithiated Graphite and Electrolyte in Lithium-Ion Battery. *J. Energy Chem.* **2022**, *69*, 593–600. [\[CrossRef\]](#)
- Huang, Z.; Shen, T.; Jin, K.; Sun, J.; Wang, Q. Heating Power Effect on the Thermal Runaway Characteristics of Large-Format Lithium Ion Battery with Li(Ni_{1/3}Co_{1/3}Mn_{1/3})O₂ as Cathode. *Energy* **2022**, *239*, 121885. [\[CrossRef\]](#)
- Zhou, Z.; Zhou, X.; Peng, Y.; Li, L.; Cao, J.; Yang, L.; Cao, B. Quantitative Study on the Thermal Failure Features of Lithium Iron Phosphate Batteries under Varied Heating Powers. *Appl. Therm. Eng.* **2021**, *185*, 116346. [\[CrossRef\]](#)
- Zhou, Z.; Ju, X.; Zhou, X.; Yang, L.; Cao, B. A Comprehensive Study on the Impact of Heating Position on Thermal Runaway of Prismatic Lithium-Ion Batteries. *J. Power Sources* **2022**, *520*, 230919. [\[CrossRef\]](#)

26. Jin, C.; Sun, Y.; Wang, H.; Lai, X.; Wang, S.; Chen, S.; Rui, X.; Zheng, Y.; Feng, X.; Wang, H.; et al. Model and Experiments to Investigate Thermal Runaway Characterization of Lithium-Ion Batteries Induced by External Heating Method. *J. Power Sources* **2021**, *504*, 230065. [[CrossRef](#)]
27. GB 38031. Safety Requirements for Power Batteries Used in Electric Vehicles. 2020. Available online: <https://blog.csdn.net/qfmzhu/article/details/106123885> (accessed on 14 April 2024).
28. Wang, H.; Zhang, Y.; Li, W.; Gao, Z.; Zhang, B.; Ouyang, M. Experimental Study on the Cell-Jet Temperatures of Abused Prismatic Ni-Rich Automotive Batteries under Medium and High States of Charge. *Appl. Therm. Eng.* **2022**, *202*, 117859. [[CrossRef](#)]
29. Zou, K.; Chen, X.; Ding, Z.; Gu, J.; Lu, S. Jet Behavior of Prismatic Lithium-Ion Batteries during Thermal Runaway. *Appl. Therm. Eng.* **2020**, *179*, 115745. [[CrossRef](#)]
30. Jia, Z.; Song, L.; Mei, W.; Yu, Y.; Meng, X.; Jin, K.; Sun, J.; Wang, Q. The Preload Force Effect on the Thermal Runaway and Venting Behaviors of Large-Format Prismatic LiFePO₄ Batteries. *Appl. Energy* **2022**, *327*, 120100. [[CrossRef](#)]
31. Kong, D.; Zhao, H.; Ping, P.; Zhang, Y.; Wang, G. Effect of Low Temperature on Thermal Runaway and Fire Behaviors of 18650 Lithium-Ion Battery: A Comprehensive Experimental Study. *Process Saf. Environ. Prot.* **2023**, *174*, 448–459. [[CrossRef](#)]
32. Zhang, F.; Feng, X.; Xu, C.; Jiang, F.; Ouyang, M. Thermal Runaway Front in Failure Propagation of Long-Shape Lithium-Ion Battery. *Int. J. Heat Mass Transf.* **2022**, *182*, 121928. [[CrossRef](#)]

Disclaimer/Publisher's Note: The statements, opinions and data contained in all publications are solely those of the individual author(s) and contributor(s) and not of MDPI and/or the editor(s). MDPI and/or the editor(s) disclaim responsibility for any injury to people or property resulting from any ideas, methods, instructions or products referred to in the content.